The Astronomical Journal, 161:47 (16pp), 2021 January https://doi.org/10.3847/1538-3881/abca39

Physical Parameters of the Multiplanet Systems HD 106315 and GJ 9827*†

Molly R. Kosiarek[1,35], David A. Berardo[2], Ian J. M. Crossfield[3], Cesar Laguna[1,4], Caroline Piaulet[5], Joseph M. Akana Murphy[1,35], Steve B. Howell[6], Gregory W. Henry[7], Howard Isaacson[8,9], Benjamin Fulton[10], Lauren M. Weiss[11], Erik A. Petigura[12], Aida Behmard[13], Lea A. Hirsch[14], Johanna Teske[15], Jennifer A. Burt[16], Sean M. Mills[17], Ashley Chontos[18,35], Teo Močnik[19], Andrew W. Howard[17], Michael Werner[16], John H. Livingston[20], Jessica Krick[21], Charles Beichman[22], Varoujan Gorjian[16], Laura Kreidberg[23,24], Caroline Morley[25], Jessie L. Christiansen[21], Farisa Y. Morales[16], Nicholas J. Scott[6], Jeffrey D. Crane[26], Sharon Xuesong Wang[27,28], Stephen A. Shectman[26], Lee J. Rosenthal[17], Samuel K. Grunblatt[29,30], Ryan A. Rubenzahl[17,35], Paul A. Dalba[31,36], Steven Giacalone[32], Chiara Dane Villanueva[1,4], Qingtian Liu[1,4], Fei Dai[13], Michelle L. Hill[31], Malena Rice[33], Stephen R. Kane[31], and Andrew W. Mayo[32,34]

[1] Department of Astronomy and Astrophysics, University of California, Santa Cruz, CA 95064, USA; molly.kosiarek@gmail.com
[2] Department of Physics, and Kavli Institute for Astrophysics and Space Research, Massachusetts Institute of Technology, Cambridge, MA 02139, USA
[3] Department of Physics & Astronomy, University of Kansas, 1082 Malott,1251 Wescoe Hall Dr., Lawrence, KS 66045, USA
[4] Department of Physics, University of California, Santa Cruz, CA 95064, USA
[5] Department of Physics, and Institute for Research on Exoplanets, Université de Montréal, Montreal, H3T 1J4, Canada
[6] NASA Ames Research Center, Moffett Field, CA 94035, USA
[7] Center of Excellence in Information Systems, Tennessee State University, Nashville, TN 37209, USA
[8] 501 Campbell Hall, University of California at Berkeley, Berkeley, CA 94720, USA
[9] Centre for Astrophysics, University of Southern Queensland, Toowoomba, QLD, Australia
[10] NASA Exoplanet Science Institute/Caltech-IPAC, MC 314-6, 1200 E. California Blvd., Pasadena, CA 91125, USA
[11] Institute for Astronomy, University of Hawai'i, 2680 Woodlawn Dr., Honolulu, HI 96822, USA
[12] Department of Physics & Astronomy, University of California Los Angeles, Los Angeles, CA 90095, USA
[13] Division of Geological and Planetary Sciences, California Institute of Technology, Pasadena, CA 91125, USA
[14] Kavli Institute for Particle Astrophysics and Cosmology, Stanford University, Stanford, CA, USA
[15] Earth & Planets Laboratory, Carnegie Institution of Washington, 5241 Broad Branch Rd., NW, Washington, DC 20015, USA
[16] Jet Propulsion Laboratory, California Institute of Technology, 4800 Oak Grove Dr., Pasadena, CA 91109, USA
[17] Department of Astronomy, California Institute of Technology, Pasadena, CA 91125, USA
[18] Institute for Astronomy, University of Hawai'i,, Honolulu, HI 96822, USA
[19] Gemini Observatory/NSF's NOIRLab, 670 N. A'ohoku Place, Hilo, HI 96720, USA
[20] Department of Astronomy, University of Tokyo, 7-3-1 Hongo, Bunkyo-ku, Tokyo 113-0033, Japan
[21] Caltech/IPAC, 1200 E. California Blvd., Pasadena, CA 91125, USA
[22] IPAC/NASA Exoplanet Science Institute, Caltech, Jet Propulsion Laboratory, USA
[23] Max Planck Institute for Astronomy, Königstuhl 17, D-69117 Heidelberg, Germany
[24] Center for Astrophysics | Harvard & Smithsonian, 60 Garden St., Cambridge, MA 02138, USA
[25] University of Texas at Austin, Austin, TX 78712, USA
[26] The Observatories of the Carnegie Institution for Science, 813 Santa Barbara St., Pasadena, CA 91107, USA
[27] Observatories of the Carnegie Institution for Science, 813 Santa Barbara St., Pasadena, CA 91101, USA
[28] Department of Astronomy, Tsinghua University, Beijing 100084, People's Republic of China
[29] American Museum of Natural History, 200 Central Park West, Manhattan, NY 10024, USA
[30] Center for Computational Astrophysics, Flatiron Institute, 162 5th Ave., Manhattan, NY 10010, USA
[31] Department of Earth and Planetary Sciences, University of California, Riverside, CA 92521, USA
[32] Department of Astronomy, University of California Berkeley, Berkeley, CA 94720-3411, USA
[33] Department of Astronomy, Yale University, New Haven, CT 06511, USA
[34] Centre for Star and Planet Formation, Natural History Museum of Denmark & Niels Bohr Institute, University of Copenhagen, Øster Voldgade 5-7, DK-1350 Copenhagen K., Denmark

Received 2020 September 7; revised 2020 November 9; accepted 2020 November 11; published 2020 December 31

Abstract

HD 106315 and GJ 9827 are two bright, nearby stars that host multiple super-Earths and sub-Neptunes discovered by K2 that are well suited for atmospheric characterization. We refined the planets' ephemerides through Spitzer transits, enabling accurate transit prediction required for future atmospheric characterization through transmission spectroscopy. Through a multiyear high-cadence observing campaign with Keck/High Resolution Echelle Spectrometer and Magellan/Planet Finder Spectrograph, we improved the planets' mass measurements in anticipation of Hubble Space Telescope transmission spectroscopy. For GJ 9827, we modeled activity-induced radial velocity signals with a Gaussian process informed by the Calcium II H&K lines in order to more accurately model the effect of stellar noise on our data. We measured planet masses of $M_b = 4.87 \pm 0.37\ M_\oplus$, $M_c = 1.92 \pm 0.49\ M_\oplus$, and $M_d = 3.42 \pm 0.62\ M_\oplus$. For HD 106315, we found that such activity radial velocity decorrelation was not effective due to the reduced presence of spots

∗ Based on observations obtained at the W. M. Keck Observatory, which is operated jointly by the University of California and the California Institute of Technology.

† This paper includes data gathered with the 6.5 meter Magellan Telescopes located at Las Campanas Observatory, Chile.

[35] NSF Graduate Research Fellow.

[36] NSF Astronomy and Astrophysics Postdoctoral Fellow.

and speculate that this may extend to other hot stars as well ($T_{\rm eff} > 6200$ K). We measured planet masses of $M_b = 10.5 \pm 3.1\ M_\oplus$ and $M_c = 12.0 \pm 3.8\ M_\oplus$. We investigated all of the planets' compositions through comparison of their masses and radii to a range of interior models. GJ 9827 b and GJ 9827 c are both consistent with a 50/50 rock-iron composition, GJ 9827 d and HD 106315 b both require additional volatiles and are consistent with moderate amounts of water or hydrogen/helium, and HD 106315 c is consistent with a ~10% hydrogen/helium envelope surrounding an Earth-like rock and iron core.

Unified Astronomy Thesaurus concepts: Radial velocity (1332); Exoplanets (498); Mini Neptunes (1063); Transit photometry (1709); Gaussian Processes regression (1930); Super Earths (1655)

Supporting material: machine-readable tables

1. Introduction

Small planets cover a wide variety of compositions ranging from dense, iron-rich planets to low density planets with large hydrogen/helium envelopes. Mass and radius are degenerate with many potential compositions; measurements of atmospheric compositions can help break this degeneracy (Figueira et al. 2009; Rogers & Seager 2010).

In this paper, we characterize two planetary systems, HD 106315 and GJ 9827. These systems both consist of multiple planets transiting bright, nearby host stars. Both systems contain promising targets for atmospheric composition studies through transmission spectroscopy. Three of the planets are being observed by the Hubble Space Telescope (HST) to study their atmospheres in GO-15333 (Kreidberg et al. 2020, Benneke et al. 2020, in preparation) and GO-15428 (Hedges et al. 2020, in preparation). These three planets are additionally compelling targets for the James Webb Space Telescope (JWST) as determined by their transmission spectroscopy metric values (TSM; Kempton et al. 2018; HD 106315 c: 91; GJ 9827 b: 95; GJ 9827 d: 144). Precise mass measurements (20% precision) are needed to support the ongoing HST analyses and potential JWST observations as mass directly affects the observability of features and inferred properties from spectra (Batalha et al. 2019).

We measure the planet radii and update their ephemerides with Spitzer transit observations in Section 2. We describe our spectroscopy, imaging data, and update stellar parameters in Section 3. We investigate stellar activity in our radial velocity observations, K2 photometry, and ground-based photometry in Section 4. We refine the planet masses through radial velocity analyses and explore the stability of including non-zero eccentricities with *N*-body simulations in Section 5. Finally, we examine potential interior compositions in Section 6 by comparing the masses and radii with composition models, before concluding in Section 7.

1.1. GJ 9827

GJ 9827 (K2-135) is a bright ($V = 10.3$ mag, $K = 7.2$ mag), nearby (distance = 30 pc) K6 dwarf star hosting three planets discovered in K2 Campaign 12 (Niraula et al. 2017; Rodriguez et al. 2018). Planets b and c orbit near a 3:1 resonance at 1.2 days and 3.6 days, with planet d at 6.2 days. These three planets span the gap seen in the radius distribution of small planets (Fulton et al. 2017) sized at $1.529 \pm 0.058\ R_\oplus$, $1.201 \pm 0.046\ R_\oplus$, and $1.955 \pm 0.075\ R_\oplus$ respectively. Niraula et al. (2017) additionally collected seven radial velocity observations with the FIbrefed Echelle Spectrograph (FIES; Frandsen & Lindberg 1999; Telting et al. 2014) to vet the system and to derive stellar parameters.

The mass of planet b was first determined with radial velocity observations from the Carnegie Planet Finder Spectrograph (PFS; Crane et al. 2006, 2008, 2010) on Magellan II by Teske et al. (2018; $M_b \sim 8\ M_\oplus$), who placed upper limits on planets c and d ($M_c < 2.5\ M_\oplus$, $M_d < 5.6\ M_\oplus$). Through additional measurements with the High Accuracy Radial velocity Planet Searcher (HARPS; Mayor et al. 2003) and the HARPS for the Northern hemisphere (HARPS-N), Prieto-Arranz et al. (2018) determined the masses of all three planets ($M_b = 3.74 \pm 0.50\ M_\oplus$, $M_c = 1.47 \pm 0.59\ M_\oplus$, and $M_d = 2.38 \pm 0.71\ M_\oplus$). The masses of planets b and d were further refined by Rice et al. (2019) with new HARPS-N radial velocity measurements and a Gaussian process informed by the K2 light curve ($M_b = 4.91 \pm 0.49\ M_\oplus$ and $M_d = 4.04 \pm 0.84\ M_\oplus$). Both Prieto-Arranz et al. (2018) and Rice et al. (2019) discuss how the inner planets have high densities and the outer planet has a lower density, suggesting that photoevaporation or migration could have played a role in the evolution of this system; we discuss this possibility further in Section 6.

1.2. HD 106315

HD 106315 (K2-109) is a bright ($V = 8.97$ mag, $K = 7.85$ mag) F5 dwarf star hosting two planets discovered in K2 Campaign 10 (Crossfield et al. 2017; Rodriguez et al. 2017). Planet b is a small ($R_b = 2.40 \pm 0.20\ R_\oplus$) planet with an orbital period of 9.55 days; planet c is a warm Neptune-sized ($R_c = 4.379 \pm 0.086\ R_\oplus$) planet with an orbital period of 21.06 days.

This system was further characterized with HARPS radial velocity observations by Barros et al. (2017) to determine the planets' masses ($M_b = 12.6 \pm 3.2\ M_\oplus$ and $M_c = 15.2 \pm 3.7\ M_\oplus$). They concluded that HD 106315 b likely has a rocky core and a decent water mass fraction whereas HD 106315 c has a substantial hydrogen-helium envelope.

Additional transits of HD 106315 c were observed with two ground-based facilities: the Euler telescope (Lendl et al. 2017) and the Cerro Tololo Inter-American Observatory (Barros et al. 2017). These measurements improved the precision on both the orbital period and the time of transit.

Later Zhou et al. (2018) investigated the system architecture through measuring the obliquity of HD 106315 c using Doppler tomography and constraining the mutual inclination of HD 106315 b through dynamical arguments. They found that these two planets both have low obliquities, consistent with the few other warm Neptunes with measured obliquities (e.g., Albrecht et al. 2013).

2. Spitzer Transits

Predicting precise future transit times becomes harder as more time elapses from previous transit observations and the uncertainty from the orbital period compounds. These systems contain promising targets for future atmospheric follow-up which require small uncertainties on the predicted transit time.

Table 1
Spitzer Transit Results

Planet	Date (UT)	Time of Conjunction (BJD)	R_p/R_* (4.5 μm)	Semimajor Axis (R_*)	Inclination (°)	Uncertainty (dex)
GJ 9827 b	2018 Mar 10	$2457738.82384^{+0.00081}_{-0.00080}$	$0.0225^{+0.0018}_{-0.0017}$	$7.19^{+0.56}_{-0.40}$	$87.7^{+1.8}_{-1.6}$	$-3.152^{+0.012}_{-0.012}$
GJ 9827c	2018 Mar 6	$2457742.1993^{+0.0025}_{-0.0028}$	$0.0201^{+0.0023}_{-0.0020}$	$13.0^{+1.7}_{-1.3}$	$88.5^{+1.4}_{-1.1}$	$-3.307^{+0.015}_{-0.017}$
GJ 9827 d	2018 Mar 28	$2457740.98800^{+0.00064}_{-0.00055}$	$0.0348^{+0.0014}_{-0.0013}$	$21.8^{+2.5}_{-1.6}$	$87.72^{+0.37}_{-0.21}$	$-3.295^{+0.017}_{-0.018}$
HD 106315 b	2017 Apr 19	$2457586.5394^{+0.0056}_{-0.0109}$	$0.0201^{+0.0026}_{-0.0024}$	$16.4^{+5.1}_{-3.1}$	$88.4^{+2.3}_{-1.1}$	$-3.197^{+0.013}_{-0.013}$
HD 106315 b	2017 Sep 10	$2457586.5826^{+0.0121}_{-0.0043}$	$0.0219^{+0.0034}_{-0.0026}$	$10.4^{+2.2}_{-1.3}$	$87.6^{+3.0}_{-1.7}$	$-3.155^{+0.010}_{-0.010}$
HD 106315 c	2017 Apr 20	$2457569.0103^{+0.0012}_{-0.0012}$	$0.0329^{+0.0013}_{-0.0012}$	$29.5^{+5.7}_{-4.2}$	$88.89^{+0.69}_{-0.51}$	$-3.189^{+0.012}_{-0.012}$

Therefore, we collected additional transit observations on the Spitzer Space Telescope to refine the ephemerides for each planet as well as to provide a depth measurement at 4.5 μm. These observations were taken as part of the K2 follow-up program 13052 (PI: Werner), using the 4.5 μm channel of IRAC (Fazio et al. 2004). A single transit of each planet was observed, except for HD 106315 b which was observed twice. All of the observations were collected with 0.4 second exposures and the target was placed on the "sweet spot" of the detector.

We follow a similar analysis approach to that described in Berardo et al. (2019), which detrends the data using the pixel level decorrelation method outlined in Deming et al. (2015). In brief, we first applied a median filter to each pixel in the image and calculated a background level for each frame by taking the median of the flux in an annulus centered on the point-spread function. We estimated the centroid of each frame by fitting a two-dimensional Gaussian to the image, and obtained a light curve using a fixed radius aperture. We varied the aperture size and performed a linear regression to determine the optimal radius; we found 2.4 pixels minimized the rms of the residuals for all observations.

We modeled systematics in the light curve by weighting the nine brightest pixels individually as well as fitting for a quadratic time ramp. We then chose the combination of pixel coefficients, aperture size, and time-series binning that resulted in the smallest rms deviation. We ran a Markov Chain Monte Carlo (MCMC) analysis to estimate parameter uncertainties, using the systematic model in addition to a transit signal which we modeled using `batman` (Kreidberg 2015). We fixed the period of each planet to the most recent measurements (Barros et al. 2017; Rice et al. 2019) and allowed the transit depth, center, orbital inclination, and semimajor axis to vary. We also left the uncertainty of the data points as a free parameter, which we found converged to the rms scatter of the raw light curve. We held fixed the quadratic limb-darkening parameters, which were determined using the tables of Claret & Bloemen (2011). The fit results are shown in Table 1 and Figure 1.

We calculated updated ephemerides (Table 2) to further refine the time of conjunction and orbital period for future atmospheric follow-up and to better constrain these values in our radial velocity fits (Section 5). We fit a straight line to the transit centers obtained from each individual observation, incorporating all ground-based published transits thus far (Lendl et al. 2017; Barros et al. 2017). These planets will be accessible for future transmission spectroscopy observations throughout the JWST era. As an example, the transit time uncertainty in 2025 is under two hours for all five planets (GJ 9827 b: 0.1 hr; GJ 9827 c: 0.5 hr; GJ 9827 d: 0.1 hr; HD 106315 b: 1.7 hr; and HD 106315 c: 0.4hr).

3. Stellar Parameters and Companion Refinement

3.1. Spectroscopy

We collected radial velocity measurements of GJ 9827 and HD 106315 with the High Resolution Echelle Spectrometer (HIRES; Vogt et al. 1994) on the Keck I Telescope on Maunakea. These exposures were taken through an iodine cell for wavelength calibration (Butler et al. 1996). The HIRES data collection, reduction, and analysis followed the California Planet Search method described in Howard et al. (2010).

We obtained 92 measurements of GJ 9827 with HIRES between 2017 September 22 and 2020 January 8 (Table 3). These data were collected with the C2 decker ($14'' \times 0\farcs861$, resolution = 50 k) with a typical signal-to-noise ratio (S/N) of 200/pixel (250k on the exposure meter, median exposure time of 18.5 minutes). We also collected a higher resolution template observation with the B3 decker ($14'' \times 0\farcs574$, resolution = 67 k) on 2017 December 30 with an S/N of 200/pixel without the iodine cell. Both the C2 and B3 decker allow for sky subtraction, which is important for the quality of the radial velocities for a $V = 10$ mag star. We included an additional 142 measurements in our GJ 9827 analysis, for a total of 234 measurements: 7 from FIES (Niraula et al. 2017), 36 from PFS (Teske et al. 2018), 35 from HARPS (Prieto-Arranz et al. 2018), and 64 from HARPS-N (Prieto-Arranz et al. 2018; Rice et al. 2019).

We obtained 352 measurements of HD 106315 with HIRES between 2016 December 23 and 2020 February 1 (Table 4); 53 of these observations were previously published in Crossfield et al. (2017). These data were collected with the B5 decker ($3\farcs5 \times 0\farcs861$, resolution = 50 k) with a typical S/N of 200/pixel (250k on the exposure meter, median exposure time of 4.8 minutes). Data were typically taken in groups of three consecutive observations to mitigate p-mode oscillations; Barros et al. (2017) estimated p-mode periods of ~20 minutes whereas Chaplin et al. (2019) estimate timescales to be ~30 minutes. When possible, multiple visits separated by an hour were taken to improve precision due to the high $v \sin i$; these data were then binned in nightly bins to average over short-timescale activity. We also collected a higher resolution template observation with the B3 decker on 2016 December 24. The template was a triple exposure with a total S/N of 346/pixel (250k each on the exposure meter) without the iodine cell.

We obtained 25 measurements of HD 106315 with PFS between 2017 January 6 and 2018 June 30 (Table 4). Data taken prior to 2018 February were taken with the $0\farcs5$ slit (resolution~80k); a single observation with an exposure time of 10 to 25 minutes was taken per night. After a PFS upgrade in 2018 February, multiple exposures were taken with the $0\farcs3$ slit (resolution ~130k). As with the HIRES data, we binned these consecutive observations for our analysis. An iodine-free

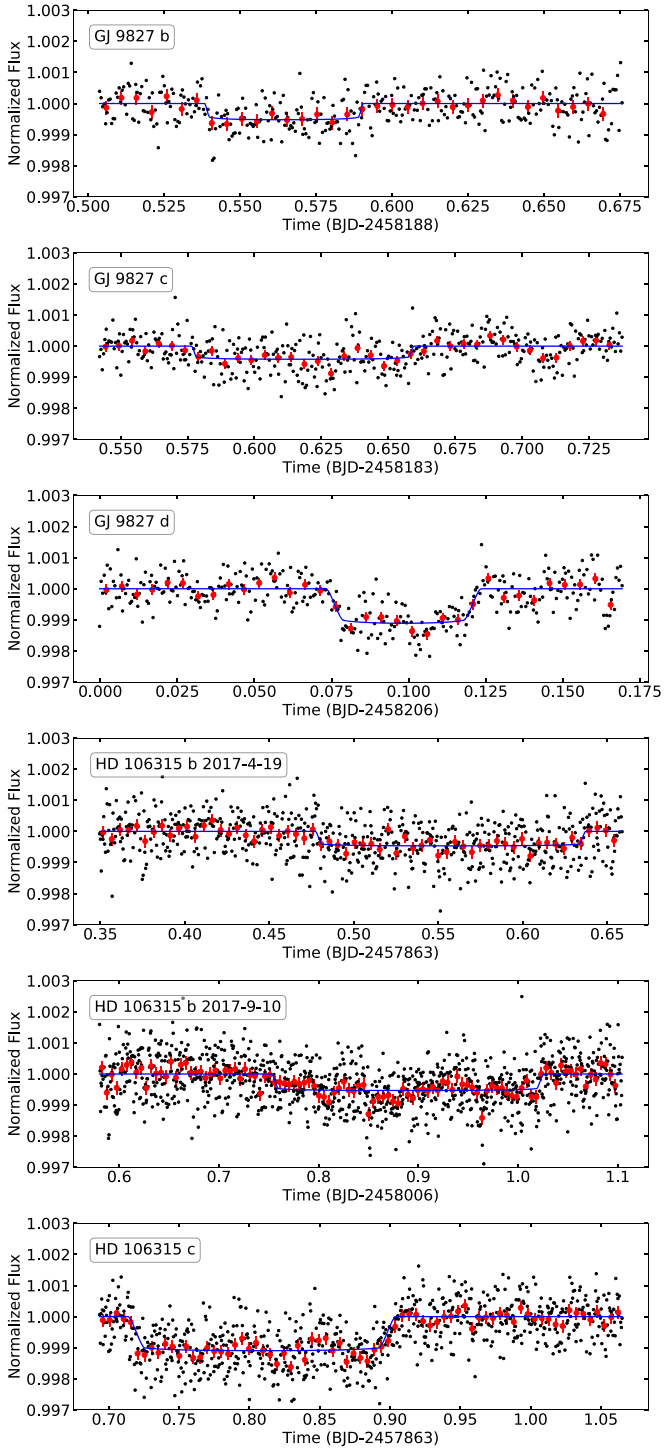

Figure 1. Spitzer transits for GJ 9827 b, c, and d and HD 106315 b and c. The data (black points), binned data (red circles), and model fit (blue line) are shown.

template, consisting of three 1000 s exposures, was taken with the 0.″3 slit on 2018 June 27. The PFS data were reduced using a custom IDL pipeline and velocities extracted based on the methodology described in Butler et al. (1996).

We additionally include 84 measurements from HARPS (Barros et al. 2017), for a total of 461 measurements (160 binned points) in our HD 106315 analysis. We collected 125 measurements on the Automated Planet Finder (APF; Radovan et al. 2014; Vogt et al. 2014) but do not include them in the analysis due to the high scatter (30 m s^{-1} nightly rms, 7.3 m s^{-1} radial velocity uncertainty), listed in Table 4.

Table 2
Ephemerides Update

Planet	Time of Conjunction (BJD)	Period (days)
GJ 9827 b	2457738.82586 ± 0.00026	1.2089765 ± 2.3e-06
GJ 9827c	2457742.19931 ± 0.00071	3.648096 ± 2.4e-05
GJ 9827 d	2457740.96114 ± 0.00044	6.20183 ± 1.0e-05
HD 106315 b	2457586.5476 ± 0.0025	9.55287 ± 0.00021
HD 106315c	2457569.01767 ± 0.00097	21.05652 ± 0.00012

Table 3
GJ 9827 Radial Velocities

Time (BJD$_{TDB}$)	Radial Velocity (m s^{-1})	Radial Velocity Unc. (m s^{-1})	S_{HK}	H-alpha	Instrument
2458787.89755	4.67	1.16	0.5741	0.05581	HIRES
2458118.80405	−0.01	1.08	0.7945	0.05629	HIRES

Note. HIRES S_{HK} values have an uncertainty of 0.001.

(This table is available in its entirety in machine-readable form.)

Table 4
HD 106315 Radial Velocities

Time (BJD$_{TDB}$)	Radial Velocity (m s^{-1})	Radial Velocity Unc. (m s^{-1})	S_{HK}	H-alpha	Instrument
2457746.13882	−6.58	4.11	0.1392	0.03299	HIRES
2457746.14353	−3.36	4.01	0.1391	0.03294	HIRES
2457759.80567	26.08	6.79	0.1515	⋯	PFS
2457761.81934	−2.24	7.28	0.1556	⋯	PFS
2457781.06111	−5.04	13.21	0.1291	⋯	APF
2457809.02734	−30.19	22.39	0.1200	⋯	APF

Note. S_{HK} values have an uncertainty of 0.001 for HIRES data, 0.002 for APF data, and no calculated uncertainties for PFS data.

(This table is available in its entirety in machine-readable form.)

We updated the stellar parameters for GJ 9827 and HD 106315 to incorporate the latest measurements, especially the Gaia DR2 parallaxes (Gaia Collaboration et al. 2016, 2018; Luri et al. 2018). We used multiband stellar photometry (Gaia G and Two Micron All-Sky Survey JHK), the Gaia parallax, and a stellar effective temperature and metallicity derived from Keck/HIRES spectra via the SpecMatch-Emp tool (Yee et al. 2017). The SpecMatch-Emp values are $T_{\rm eff} = 6318 \pm 110$ K and 4195 ± 70 K, and [Fe/H] $= -0.21 \pm 0.09$ and -0.29 ± 0.09 for HD 106315 and GJ 9827, respectively. We input the above values into the isoclassify tool using the grid-mode option (Huber et al. 2017) to derive the stellar parameters listed in Table 5.

3.2. HD 106315 Imaging

The discovery papers for HD 106315 included seeing-limited imaging data and *K*-band Keck/NIRC2 infrared adaptive optics imaging to rule out nearby stellar companions

Table 5
Stellar Parameters

Parameter	Units	GJ 9827	HD 106315
[Fe/H]	dex	-0.26 ± 0.08	-0.22 ± 0.09
M_*	$M_{\rm Sun}$	0.593 ± 0.018	1.154 ± 0.042
R_*	$R_{\rm Sun}$	0.579 ± 0.018	1.269 ± 0.024
log g	dex	4.682 ± 0.021	4.291 ± 0.025
$T_{\rm eff}$	K	4294 ± 52	6364 ± 87

(Rodriguez et al. 2017; Crossfield et al. 2017). We include here additional high-contrast imaging data to improve the magnitude contrast constraints on nearby companions.

We observed HD 106315 on 2019 June 20 UT using the Zorro speckle interferometric instrument[37] mounted on the 8 m Gemini South telescope located on the summit of Cerro Pachon in Chile. Zorro simultaneously observes in two bands, one centered at 832 nm with a width of 40 nm and the other centered at 562 nm with a width of 54 nm, obtaining diffraction-limited images with inner working angles 0.″017 and 0.″026, respectively. Our data set consisted of 3 minutes of total integration time taken as sets of 1000×0.06 sec images. All the images were combined and subjected to Fourier analysis leading to the production of final data products including speckle reconstructed imagery (see Howell et al. 2011). Figure 2 shows the 5σ contrast curves in both filters for the Zorro observation and includes an inset showing the 832 nm reconstructed image. The speckle imaging results confirm HD 106315 to be a single star to contrast limits of 5–8.6 magnitudes, ruling out main-sequence companions fainter than HD 106315 itself within the spatial limits of 2 to 125 au.

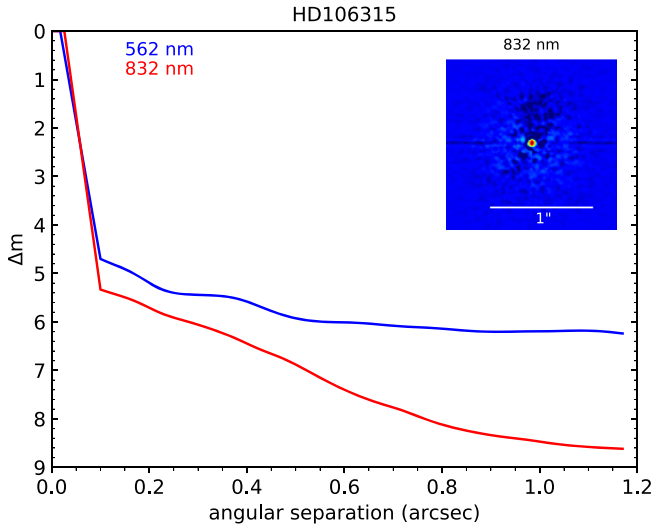

Figure 2. Gemini-S/Zorro speckle-imaging contrast curve for HD 106315 in 832 nm (red) and 562 nm (blue) including an inset image of the 832 nm observation. No stellar companions or background sources are seen in these data.

4. Stellar Activity Analysis

Variability in the brightness and velocity fields across the stellar disk results in line shape variations and apparent radial velocity shifts. Stellar activity with timescales comparable to planet orbital periods is a particular problem for radial velocity analyses as these signals can appear as additional Keplerian signals or can affect the fit amplitudes of the planet signals (e.g., Fulton et al. 2015). For our two systems, we focus on the component of stellar activity related to stellar rotation, as these signals have similar timescales to the transiting planet signals.

Stellar activity can be tracked in radial velocity data using certain stellar lines as activity indicators. The Calcium II H&K lines are often used for this purpose ($S_{\rm HK}$; Isaacson & Fischer 2010), whereas Hα may be more successful for cooler stars (Robertson et al. 2013). Another method is to use photometry to characterize the stellar activity and then subsequently fold the activity information into radial velocity fits (Haywood et al. 2014). For the Sun, there is a connection between stellar activity information derived from photometry, activity indicators, and radial velocity data (Kosiarek & Crossfield 2020). Here we investigate how stellar activity manifests in the K2 light curve, the Calcium II H&K and Hα stellar lines, and our radial velocity data.

4.1. GJ 9827 Stellar Activity

The K2 light curve for GJ 9827 shows quasi-periodic variation with signs of active region evolution between rotation cycles (Figure 3). The K2 photometry shown in this paper was produced using k2phot (Petigura et al. 2015, 2017). A Lomb–Scargle periodogram of the K2 data shows two strong peaks around 15 and 30 days consistent with previous works, one peak is likely the rotation period and the other a harmonic. We consider both peaks since stellar rotation periods often do not appear as the highest peak in a periodogram (Nava et al. 2020). The shorter period is favored by Niraula et al. (2017) from the $v \sin i$ measurement, whereas the longer period is favored by Rodriguez et al. (2018), Teske et al. (2018), Prieto-Arranz et al. (2018), and Rice et al. (2019) from a combination of periodogram, autocorrelation, and Gaussian process analyses on the light curve as well as from the inferred age of GJ 9827.

The Keck/HIRES $S_{\rm HK}$ and radial velocity data shown in Figure 3 both reveal a tenuous stellar rotation signal at 30 days, consistent with the longer peak in the K2 light curve periodogram. In agreement with previous findings, we conclude that this 30 day signal is likely caused by stellar rotation, as it is present in both the $S_{\rm HK}$ data and the photometry. Since there is power at the same period in our radial velocity data, we need to account for this signal in our radial velocity analysis in order to derive accurate mass measurements for the planets. We mitigated this signal using a Gaussian process, as described below in Section 5.1.

4.2. HD 106315 Stellar Activity

Similar to GJ 9827, we aim to understand the stellar activity component of the radial velocity data through investigating the possible relationships between the K2 light curve, the Calcium II H&K, and Hα stellar lines, and our radial velocity data. The projected rotational velocity measurement ($v \sin i = 13.2 \pm 1\,{\rm km\,s^{-1}}$) combined with the obliquity measurement ($\lambda = -10.9 \pm 3.7$; Zhou et al. 2018) suggest a stellar rotation period of 4.78 ± 0.15 days.

HD 106315 was observed in K2 Campaign 10; this campaign had a 14 day data gap resulting in 49 days of contiguous data. With a 4.8 day rotation period, the shorter campaign should not impact our conclusions about stellar activity from this photometry. The K2 light curve (Figure 4)

[37] https://www.gemini.edu/sciops/instruments/alopeke-zorro/

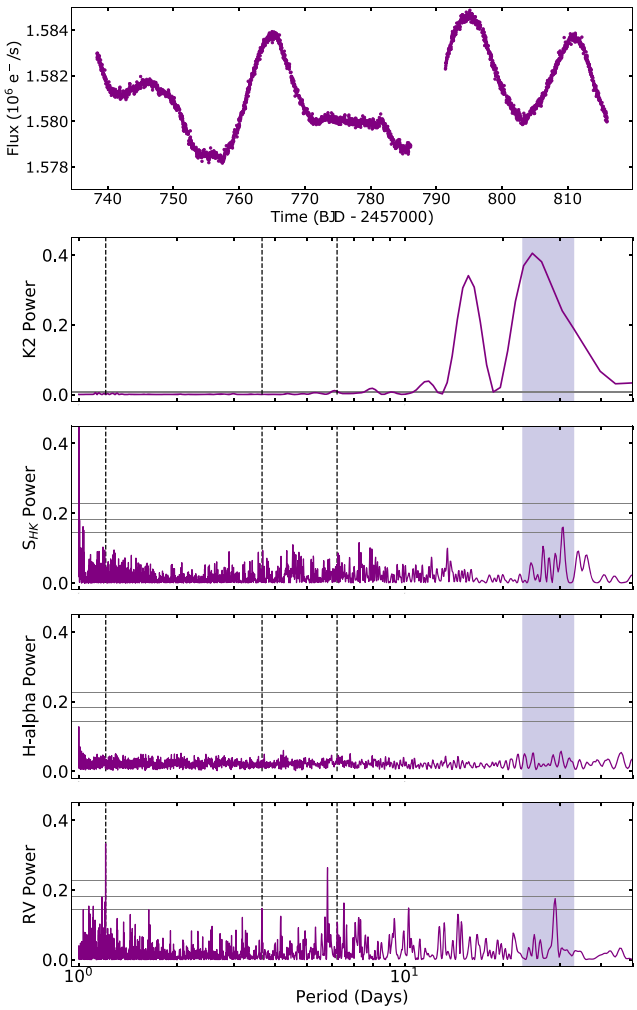

Figure 3. Activity analysis for GJ 9827 from K2 photometry and HIRES spectroscopy. There are clear stellar rotation and active region evolution signals visible by eye in the K2 photometry. The Lomb–Scargle periodograms of the K2 photometry, $S_{\rm HK}$, Hα, and radial velocity data include false-alarm probabilities of 0.5, 0.1, and 0.01 (horizontal lines), stellar rotation (blue shaded area), and planet orbital periods (dashed lines). There is a stellar rotation signal at 30 days in the $S_{\rm HK}$ and radial velocity data, consistent with the broad peak in the K2 photometry.

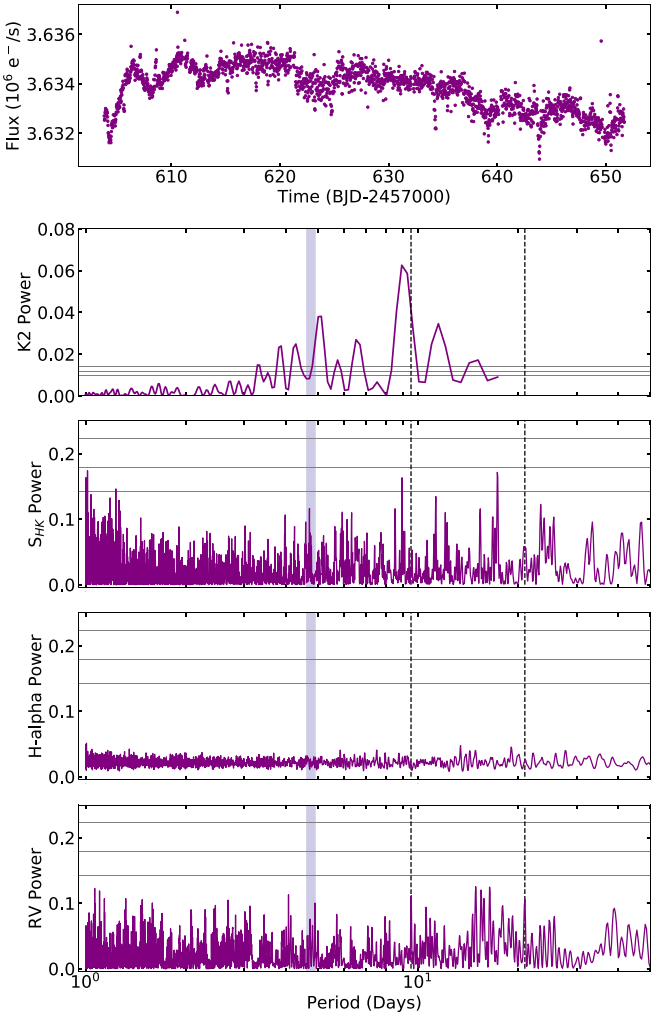

Figure 4. Activity analysis for HD 106315 from K2 photometry and HIRES spectroscopy. The Lomb–Scargle periodograms of the photometry, $S_{\rm HK}$, Hα, and radial velocity data include false-alarm probabilities of 0.5, 0.1, and 0.01 (horizontal lines), stellar rotation period (thick blue line), and planet orbital periods (dashed lines). There are peaks near the rotation period and second harmonic in the K2 photometry, and we find no similar peaks in the HIRES activity indicators or radial velocity data.

has low photometric variability; the periodogram shows a small peak near the stellar rotation period at 4.8 days and a larger peak at the second harmonic of the rotation period at 9.6 days.

We next investigated the potential radial velocity signal from the stellar rotation by examining the $S_{\rm HK}$ and Hα data in the HIRES spectra (Table 4). We find no significant peaks near 4.8 days or elsewhere in the Lomb–Scargle periodograms of the HIRES activity indicators and radial velocity data (Figure 4). The absence of these signals suggests that the stellar rotation is not contributing a significant stellar activity signal to the radial velocity measurements, potentially attributed to the low spot coverage of this F star (<1%; Kreidberg et al. 2020).

4.3. Ground-based Photometry

Stellar photometry of both systems was collected from the Fairborn Observatory in Arizona to lengthen the photometry baseline from which to look for stellar variability.

Table 6
GJ 9827 Photometry

Time (HJD)	ΔR_C (mag)
2458384.8398	−3.29860
2458387.7886	−3.29043

(This table is available in its entirety in machine-readable form.)

Table 7
HD 106315 Photometry

Time (HJD)	$\Delta((b+y)/2$ (mag)
2458159.9462	1.58370
2458161.9455	1.58287

(This table is available in its entirety in machine-readable form.)

Photometry of GJ 9827 was collected with the Tennessee State University Celestron C14 0.36 m Automated Imaging Telescope (AIT; Henry 1999; Eaton et al. 2003). A total of 74

Table 8
GJ 9827 Radial Velocity Fit Parameters

Parameter	Name (Units)	Keplerian Fit	Gaussian Process Fit (Adopted)
Orbital Parameters			
P_b	Period (days)	$1.2089765^{+2.2e-06}_{-2.3e-06}$	$1.2089765 \pm 2.3e-06$
$T\mathrm{conj}_b$	Time of Conjunction (BJD)	$2457738.82586 \pm 0.00026$	$2457738.82586 \pm 0.00026$
R_b	Radius ($R_\oplus$)	$\equiv 1.529 \pm 0.058$	$\equiv 1.529 \pm 0.058$
e_b	Eccentricity	$\equiv 0.0$	$\equiv 0.0$
ω_b	Argument of Periapse	$\equiv 0.0$	$\equiv 0.0$
K_b	Semi-amplitude (m s^{-1})	3.5 ± 0.32	4.1 ± 0.3
a_b	Semimajor Axis (AU)	0.01866 ± 0.00019	0.01866 ± 0.00019
M_b	Mass ($M_\oplus$)	$4.12^{+0.39}_{-0.38}$	4.87 ± 0.37
ρ_b	Density (g cm^{-3})	$6.32^{+1.0}_{-0.87}$	$7.47^{+1.1}_{-0.95}$
P_c	Period (days)	$3.648095^{+2.5e-05}_{-2.4e-05}$	$3.648095 \pm 2.4e-05$
$T\mathrm{conj}_c$	Time of Conjunction (BJD)	$2457742.19927 \pm 0.00071$	$2457742.19929^{+0.00072}_{-0.00071}$
R_c	Radius ($R_\oplus$)	$\equiv 1.201 \pm 0.046$	$\equiv 1.201 \pm 0.046$
e_c	Eccentricity	$\equiv 0.0$	$\equiv 0.0$
ω_c	Argument of Periapse	$\equiv 0.0$	$\equiv 0.0$
K_c	Semi-amplitude (m s^{-1})	1.28 ± 0.32	1.13 ± 0.29
a_c	Semimajor Axis (AU)	$0.03896^{+0.00039}_{-0.0004}$	$0.03896^{+0.00039}_{-0.0004}$
M_c	Mass ($M_\oplus$)	$2.17^{+0.54}_{-0.55}$	1.92 ± 0.49
ρ_c	Density (g cm^{-3})	$6.9^{+2.0}_{-1.8}$	$6.1^{+1.8}_{-1.6}$
P_d	Period (days)	$6.20183 \pm 1e-05$	$6.20183 \pm 1e-05$
$T\mathrm{conj}_d$	Time of Conjunction (BJD)	$2457740.96114 \pm 0.00044$	$2457740.96114^{+0.00045}_{-0.00044}$
R_d	Radius ($R_\oplus$)	$\equiv 1.955 \pm 0.075$	$\equiv 1.955 \pm 0.075$
e_d	Eccentricity	$\equiv 0.0$	$\equiv 0.0$
ω_d	Argument of Periapse	$\equiv 0.0$	$\equiv 0.0$
K_d	Semi-amplitude (m s^{-1})	1.63 ± 0.31	1.7 ± 0.3
a_d	Semimajor Axis (AU)	$0.0555^{+0.00056}_{-0.00057}$	$0.0555^{+0.00055}_{-0.00057}$
M_d	Mass ($M_\oplus$)	3.29 ± 0.64	3.42 ± 0.62
ρ_d	Density (g cm^{-3})	$2.41^{+0.58}_{-0.52}$	$2.51^{+0.57}_{-0.51}$
Instrument Parameters			
γ_{HIRES}	Mean Center-of-mass (m s^{-1})	$-1.87^{+0.38}_{-0.39}$	$-2.4^{+1.3}_{-1.4}$
γ_{HARPS}	Mean Center-of-mass (m s^{-1})	31946.64 ± 0.37	$31947.7^{+4.0}_{-3.6}$
$\gamma_{\mathrm{HARPS-N}}$	Mean Center-of-mass (m s^{-1})	$31948.64^{+0.43}_{-0.42}$	$31950.2^{+2.7}_{-2.6}$
γ_{PFS}	Mean Center-of-mass (m s^{-1})	0.28 ± 0.86	0.6 ± 1.2
γ_{FIES}	Mean Center-of-mass (m s^{-1})	$31775.5^{+1.1}_{-1.2}$	31775.6 ± 1.5
σ_{HIRES}	Jitter (m s^{-1})	$3.45^{+0.32}_{-0.27}$	$2.15^{+0.49}_{-0.43}$
σ_{HARPS}	Jitter (m s^{-1})	$1.65^{+0.39}_{-0.35}$	$0.91^{+0.44}_{-0.45}$
$\sigma_{\mathrm{HARPS-N}}$	Jitter (m s^{-1})	$2.79^{+0.39}_{-0.35}$	$0.74^{+0.44}_{-0.45}$
σ_{PFS}	Jitter (m s^{-1})	$4.68^{+0.75}_{-0.62}$	4.0 ± 1.1
σ_{FIES}	Jitter (m s^{-1})	$0.0001^{+0.0016}_{-0.0001}$	$0.035^{+2.6}_{-0.035}$
GP Parameters			
$\eta_{1,\mathrm{HIRES}}$	GP Amplitude (m s^{-1})	N/A	$3.7^{+1.2}_{-1.0}$
$\eta_{1,\mathrm{HARPS}}$	GP Amplitude (m s^{-1})	N/A	$5.3^{+3.5}_{-2.2}$
$\eta_{1,\mathrm{HARPS-N}}$	GP Amplitude (m s^{-1})	N/A	$5.1^{+2.3}_{-1.5}$
$\eta_{1,\mathrm{PFS}}$	GP Amplitude (m s^{-1})	N/A	4.0 ± 1.1
$\eta_{1,\mathrm{FIES}}$	GP Amplitude (m s^{-1})	N/A	$0.035^{+2.6}_{-0.035}$
η_2	Evolutionary Timescale (days)	N/A	82^{+17}_{-14}
η_3	Period of the Correlated Signal (days)	N/A	$28.62^{+0.48}_{-0.38}$
η_4	Length Scale	N/A	$0.418^{+0.082}_{-0.065}$

Note. Derived parameters use $M_* = 0.593 \pm 0.018$, $R_* = 0.579 \pm 0.019$ (this work), $R_b/R_* = 0.02420 \pm 0.00044$, $R_c/R_* = 0.01899 \pm 0.00036$, and $R_d/R_* = 0.03093 \pm 0.00062$ (Rodriguez et al. 2018).

observations were collected from 2018 September 22 to 2020 January 27 with the Cousins R filter (Table 6). The differential magnitudes were computed by subtracting the average brightness of seven comparison stars in the same field of view. A frequency spectrum of the observations show no significant periodicities between 1 and 100 days; the observations scatter about their mean with a standard deviation of 0.00372 mag.

Photometry of HD 106315 was collected with the T12 0.80 m Automatic Photoelectric Telescope (APT); the T12 APT is essentially identical in construction and operation to the T8 0.8 m APT described in Henry (1999). A total of 43

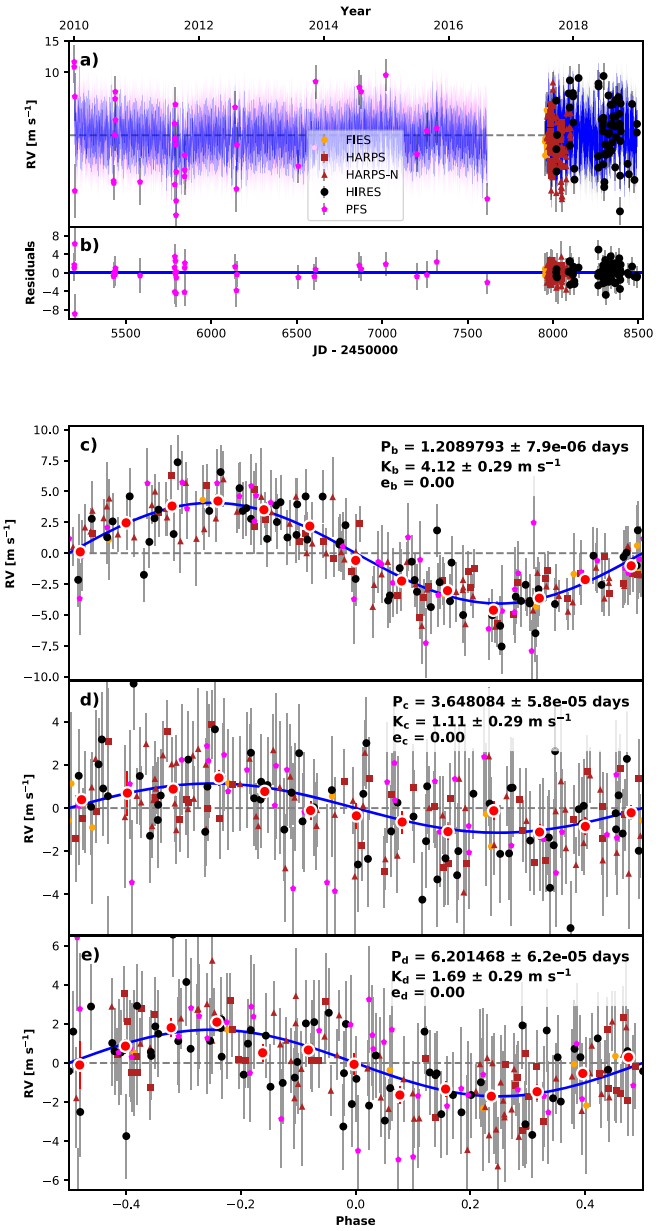

Figure 5. Best-fit three-planet Keplerian orbital model with a Gaussian process for GJ 9827. The thin blue line is the best-fit one-planet model with the mean Gaussian process model; the colored area surrounding this line includes the 1σ maximum-likelihood Gaussian process uncertainties. We add in quadrature the radial velocity jitter terms listed in Table 8 with the measurement uncertainties for all radial velocities. (b) Residuals to the best-fit two-planet model. (c) Radial velocities phase-folded to the ephemeris of planet b; the Keplerian orbit models for the other planets have been subtracted. Red circles are the same velocities binned in 0.08 units of orbital phase. (d) Radial velocities phase-folded to the ephemeris of planet c. (e) Radial velocities phase-folded to the ephemeris of planet d.

observations of HD 106315 were collected between 2018 February 9 and 2018 June 7 in both the Stromgren b and y filters by T12's two-channel photometer (Table 7). The two filters were averaged together into the $(b+y)/2$ filter to increase the data precision. The differential magnitudes were calculated using three comparison stars: HD 105374, HD 105589, and HD 106965. A frequency spectrum of the observations show no significant periodicities between 1 and 100 days; the observations scatter about their mean with a standard deviation of 0.00256 mag.

5. Radial Velocity Analysis

We analyzed the radial velocity data for these two systems with `radvel`[38] (Fulton et al. 2018). `radvel` models Keplerian orbits and optional Gaussian processes to fit radial velocity data. The fit is performed through a maximum-likelihood function and errors are determined with an MCMC analysis. We use the default number of walkers, number of steps, and criteria for burn-in and convergence as described in Fulton et al. (2018).

For both systems, we first model the radial velocity data including circular Keplerian orbits for all of the transiting planets; we include a Gaussian prior on the orbital period (P) and time of transit ($T_{\rm conj}$) from our updated ephemerides in Section 2. The semi-amplitudes (K) reported from these analyses refer to the motion of the star induced by the orbiting planet. Afterwards, we test models including a trend ($\dot{\gamma}$), curvature ($\ddot{\gamma}$), and planet eccentricities (e, ω). We used the Akaike information criterion corrected for small samples sizes (AIC) to evaluate if the fit improved sufficiently to justify the additional free parameters; a lower AIC indicates an improved fit.

5.1. Radial Velocity Analysis for GJ 9827

There is evidence of stellar activity in our radial velocity data from the periodogram analysis in Section 4. We include a Gaussian process with a quasi-periodic kernel to model this activity signal in our radial velocity fit. The kernel has the form

$$k(t,t') = \eta_1^2 \exp\left[-\frac{(t-t')^2}{\eta_2^2} - \frac{\sin^2\left(\frac{\pi(t-t')}{\eta_3}\right)}{2\eta_4^2}\right], \quad (1)$$

where the hyperparameter η_1 is the amplitude of the covariance function, η_2 is the active region evolutionary timescale, η_3 is the period of the correlated signal, and η_4 is the length scale of the periodic component. We explore these hyperparameters for this system by performing a maximum-likelihood fit to the K2 light curve, $S_{\rm HK}$, and Hα data with the quasi-periodic kernel (Equation (1)), then determine the errors through an MCMC analysis.

The K2 light curve fit is well constrained by the Gaussian process and produces a stellar rotation period consistent with the periodogram analysis of this data ($\eta_3 = 28.62^{+0.48}_{-0.38}$). The H$\alpha$ data has very low variation; it is not well fit by this kernel and does not produce meaningful posteriors.

The $S_{\rm HK}$ data is well fit by this quasi-periodic kernel and produces a stellar rotation period (η_3) consistent with our periodogram analysis in Section 4. The photometry and the $S_{\rm HK}$ data both produce consistent posteriors; we choose to adopt the posteriors from the $S_{\rm HK}$ fit because these data are taken simultaneously with the radial velocity data and are therefore a direct indicator of the chromospheric magnetic activity. The posteriors on the parameters from our $S_{\rm HK}$ fit are: $\gamma_{S_{\rm HK}} = 0.646^{+0.027}_{-0.026}$, $\sigma_{S_{\rm HK}} = 0.0183^{+0.0035}_{-0.0032}$, $\eta_1 = 0.079^{+0.017}_{-0.012}$, $\eta_2 = 94^{+50}_{-25}$ days, $\eta_3 = 29.86^{+0.78}_{-0.83}$ days, and $\eta_4 = 0.587^{+0.14}_{-0.096}$.

We then performed a Gaussian process fit on the radial velocity data including priors on η_2, η_3, and η_4 equivalent to the $S_{\rm HK}$ fit posteriors. We tested fits including a trend, curvature, and planet eccentricities but reject all of these models due to

[38] https://radvel.readthedocs.io/

Table 9
HD 106315 Radial Velocity Fit Parameters

Parameter	Name (Units)	Keplerian Fit (Adopted)	Gaussian Process Fit
Orbital Parameters			
P_b	Period (days)	9.55288 ± 0.00021	$9.55288^{+0.00019}_{-0.00021}$
$T\mathrm{conj}_b$	Time of Conjunction (BJD)	$2457586.5476^{+0.0024}_{-0.0025}$	$2457586.5479^{+0.003}_{-0.0026}$
R_b	Radius ($R_\oplus$)	$\equiv 2.40 \pm 0.20$	$\equiv 2.40 \pm 0.20$
e_b	Eccentricity	$\equiv 0.0$	$\equiv 0.0$
ω_b	Argument of Periapse	$\equiv 0.0$	$\equiv 0.0$
K_b	Semi-amplitude (m s^{-1})	$2.88^{+0.85}_{-0.84}$	$2.91^{+0.79}_{-0.85}$
a_b	Semimajor Axis (AU)	$0.0924^{+0.0011}_{-0.0012}$	$0.0924^{+0.0011}_{-0.0012}$
M_b	Mass ($M_\oplus$)	10.5 ± 3.1	$10.6^{+2.9}_{-3.1}$
ρ_b	Density (g cm^{-3})	$4.1^{+1.9}_{-1.4}$	$4.1^{+1.8}_{-1.4}$
P_c	Period (days)	21.05652 ± 0.00012	21.05653 ± 0.00012
$T\mathrm{conj}_c$	Time of Conjunction (BJD)	$2457569.01767^{+0.00097}_{-0.00096}$	$2457569.0178^{+0.0012}_{-0.001}$
R_c	Radius ($R_\oplus$)	$\equiv 4.379 \pm 0.086$	$\equiv 4.379 \pm 0.086$
e_c	Eccentricity	$\equiv 0.0$	$\equiv 0.0$
ω_c	Argument of Periapse	$\equiv 0.0$	$\equiv 0.0$
K_c	Semi-amplitude (m s^{-1})	2.53 ± 0.79	$2.61^{+0.74}_{-0.87}$
a_c	Semimajor Axis (AU)	$0.1565^{+0.0019}_{-0.002}$	$0.1565^{+0.0019}_{-0.002}$
M_c	Mass ($M_\oplus$)	12.0 ± 3.8	$12.4^{+3.5}_{-4.2}$
ρ_c	Density (g cm^{-3})	$0.78^{+0.26}_{-0.25}$	$0.81^{+0.24}_{-0.27}$
Instrument Parameters			
γ_{HIRES}	Mean Center-of-mass (m s^{-1})	$-2.48^{+0.96}_{-0.97}$	$-2.7^{+1.0}_{-1.1}$
γ_{HARPS}	Mean Center-of-mass (m s^{-1})	$-3462.94^{+0.7}_{-0.71}$	$-3462.77^{+1.1}_{-0.87}$
γ_{PFS}	Mean Center-of-mass (m s^{-1})	$-2.9^{+2.8}_{-2.7}$	$-2.5^{+3.2}_{-3.3}$
σ_{HIRES}	Jitter (m s^{-1})	$8.33^{+0.85}_{-0.79}$	$6.4^{+1.2}_{-1.1}$
σ_{HARPS}	Jitter (m s^{-1})	$2.94^{+0.94}_{-1.0}$	$2.3^{+1.0}_{-1.4}$
σ_{PFS}	Jitter (m s^{-1})	$9.4^{+2.6}_{-2.3}$	$4.0^{+4.6}_{-2.7}$
GP Parameters			
$\eta_{1,\mathrm{HIRES}}$	GP Amplitude (m s^{-1})	N/A	$5.2^{+1.1}_{-1.7}$
$\eta_{1,\mathrm{HARPS}}$	GP Amplitude (m s^{-1})	N/A	$2.3^{+1.0}_{-1.4}$
$\eta_{1,\mathrm{PFS}}$	GP Amplitude (m s^{-1})	N/A	$4.0^{+4.6}_{-2.7}$
η_2	Evolutionary Timescale (days)	N/A	$5.27^{+0.54}_{-0.65}$
η_3	Period of the Correlated Signal (days)	N/A	$4.5^{+0.49}_{-0.65}$
η_4	Length Scale	N/A	$0.56^{+0.036}_{-0.04}$

Note. Derived parameters use $M_* = 1.154 \pm 0.043$, $R_* = 1.269 \pm 0.024$ (this work), $R_b/R_* = 0.01708 \pm 0.00135$ (Crossfield et al. 2017), and $R_c/R_* = 0.031636 \pm 0.0001834$ (Kreidberg et al. 2020).

their higher AIC values. These tested fits resulted in semi-amplitudes for all three planets consistent to 1σ for planets b and d, and 2σ for planet c with the circular three-planet Gaussian process fit.

We present our GJ 9827 results in Table 8. We list the results from a circular three-planet case with and without a Gaussian process for comparison, and adopt the fit including the Gaussian process shown in Figure 5. We measure masses for these planets to be $M_b = 4.87 \pm 0.37\ M_\oplus$, $M_c = 1.92 \pm 0.49\ M_\oplus$, and $M_d = 3.42 \pm 0.62\ M_\oplus$.

5.2. Radial Velocity Analysis for HD 106315

For HD 106315, the circular two-planet fit is favored by the AIC over fits with a trend, curvature, or planet eccentricities; results are listed in Table 9 and the fit is displayed in Figure 6. In agreement with Barros et al. (2017), we do not see evidence of the trend suggested in Crossfield et al. (2017) with an AIC value 1.25 larger than the circular case. We determine masses for the HD 106315 system to be $M_b = 10.5 \pm 3.1\ M_\oplus$ and $M_c = 12.0 \pm 3.8\ M_\oplus$.

In contrast with our GJ 9827 analysis, we choose not to include a Gaussian process in our HD 106315 fit as we do not see evidence for stellar rotation induced activity contamination in the activity indicators or radial velocity data. We suspect the low spot coverage of HD 106315(<1%; Kreidberg et al. 2020) is why we see a small rotation signal in the photometry and a lack of this signal in our radial velocity data.

Barros et al. (2017) do use a Gaussian process for their analysis of HD 106315. The derived Gaussian process period is 2.8 days and their FWHM measurements also show a similar periodicity leading them to believe that this signal arises from stellar activity. At the time, Zhou et al. (2018) had not yet measured the obliquity, therefore, Barros et al. (2017) hypothesized that this 2.8 day signal was the stellar rotation period or half of the rotation period.

If this signal is associated with stellar activity, it is possible that their high-cadence radial velocity run is more sensitive to this activity than our data collection spanning multiple years. The HARPS measurements were collected on 47 nights over three months, whereas we have 94 nights of HIRES measurements over three years. It is also possible that the Gaussian

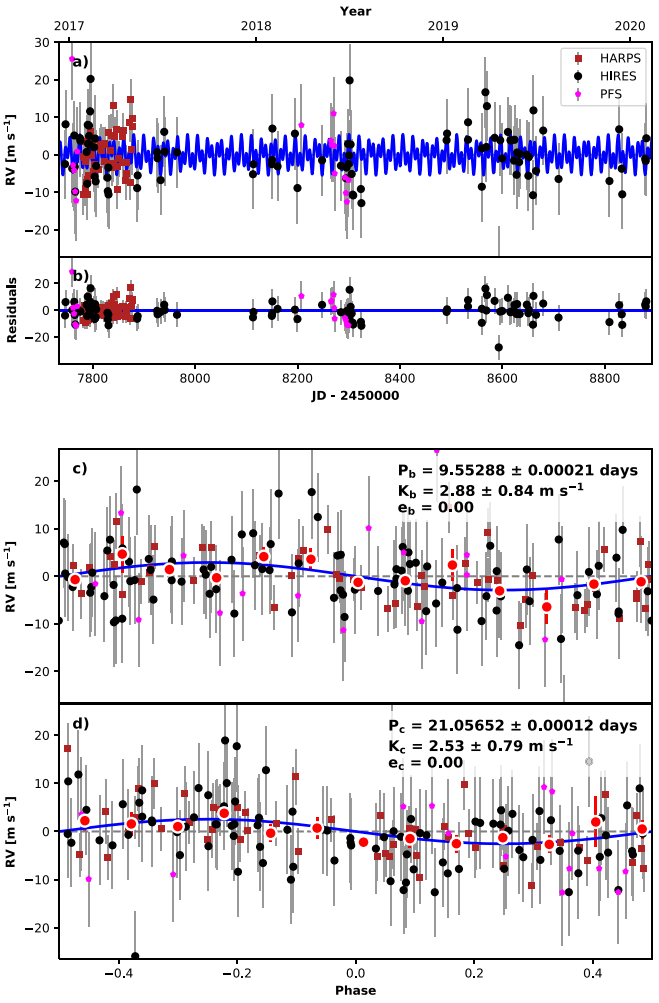

Figure 6. Best-fit two-planet Keplerian orbital model for HD 106315. The thin blue line is the best-fit two-planet model. We add in quadrature the radial velocity jitter terms listed in Table 9 with the measurement uncertainties for all radial velocities. (b) Residuals to the best-fit two-planet model. (c) Radial velocities phase-folded to the ephemeris of planet b with the orbit model of planet c subtracted. Red circles are the same velocities binned in 0.08 units of orbital phase. (d) Radial velocities phase-folded to the ephemeris of planet c.

process used by Barros et al. (2017) had fit spurious noise instead of a stellar activity signal; the 2.8 day signal is too short to be the rotation period or half of the rotation period. Hotter stars ($T_{\rm eff} > 6200$ K) often have shallow convective envelopes and inefficient magnetic dynamos which result in fewer spots on the stellar surface (Kraft 1967). Therefore, hotter stars like HD 106315 may not have enough starspots for this type of Gaussian process to be effective.

For completeness, we perform a Gaussian process fit on the HD 106315 radial velocity data. We first fit the K2 data using a Gaussian process as this data set showed periodicity at the stellar rotation period; the posteriors of this fit are: $\gamma_{K2} = 3633710^{+190}_{-200}$ e$^-$ s^{-1}, $\sigma_{K2} = 117^{+16}_{-15}$ e$^-$ s^{-1}, $\eta_1 = 655^{+84}_{-68}$ e$^-$ s^{-1}, $\eta_2 = 5.17^{+0.66}_{-0.64}$ days, $\eta_3 = 4.49^{+0.61}_{-0.26}$ days, and $\eta_4 = 0.55^{+0.04}_{-0.044}$. We then performed a Gaussian process fit on the radial velocity data including priors on η_2, η_3, and η_4 from the K2 fit posteriors. This fit results in semi-amplitudes consistent to 1σ for both planets; the full results are shown in Table 9. The Gaussian process fit has a higher AIC value (ΔAIC = 7.38) suggesting that Gaussian process parameters do not significantly improve the fit. For this reason, and as we do not see signs of stellar activity in our activity indicators or radial velocity data, we adopt the fit without a Gaussian process.

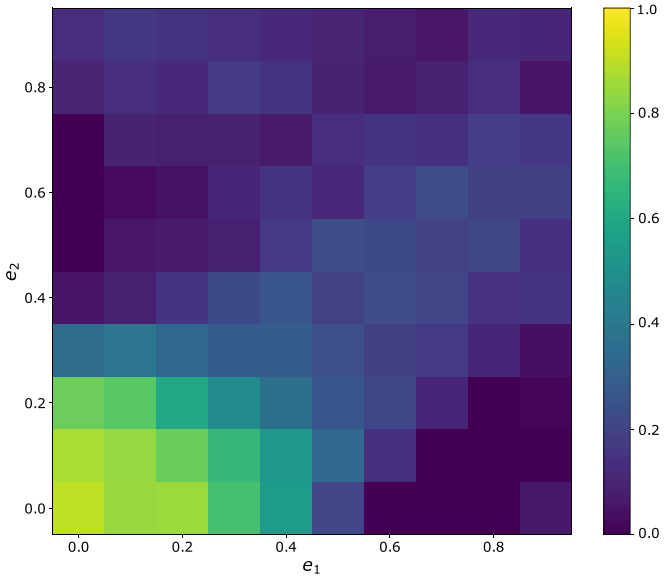

Figure 7. Probability of stability for the HD 106315 system. We examined the effect of planet eccentricity on the system's stability using `spock`. For each pair of eccentricities, we vary ω_1 and ω_2 from zero to 2π. The color of the box displays the average probability of stability across all ω.

5.3. Eccentricity Constraints

We explored the range of planet eccentricities consistent with system stability through *N*-body simulations as including eccentricity was not warranted in our radial velocity fits for either system. The literature on GJ 9827 assumed circular orbits for their fits (Prieto-Arranz et al. 2018; Rice et al. 2019). For HD 106315, Barros et al. (2017) include eccentricity terms in their radial velocity analysis resulting in $e_b = 0.1 \pm 0.1$ and $e_c = 0.22 \pm 0.15$, although they do not discuss if including the eccentricity terms improve the fit. Our eccentric radial velocity fit for HD 106315 resulted in $e_b = 0.18 \pm 0.17$ and $e_c = 0.21 \pm 0.24$, consistent with Barros et al. (2017). Though our eccentric fit had a higher AIC than the circular fit (ΔAIC = 6.22) suggesting that including eccentricity did not sufficiently improve the fit to justify the additional parameters.

We evaluated the stability of both systems using `spock` (Tamayo et al. 2020). `spock` predicts whether a given orbital configuration is stable by using `rebound` (Rein & Liu 2011) to simulate the first 10^4 orbits of a system and then calculating the probability that this system is stable for a full 10^9 orbits by comparing it to a wide sample of full simulations. These full simulations include mean-motion resonance and mutually inclined and eccentric systems; the parameters are drawn from those typically encountered in current multiplanet systems.

We initialized both systems at the maximum-likelihood values for the planet masses, orbital periods, times of conjunction, and stellar masses derived in this paper. We then varied e and ω for all planets to explore the stability of the system. For HD 106315, we varied e_1 and e_2 from 0.0 to 0.9 in steps of 0.1. At each eccentricity pair, we performed a grid of simulations varying ω_1 and ω_2 from zero to 2π in steps of $\frac{\pi}{5}$, resulting in 10,000 simulations. We then averaged over the simulated ω grid to

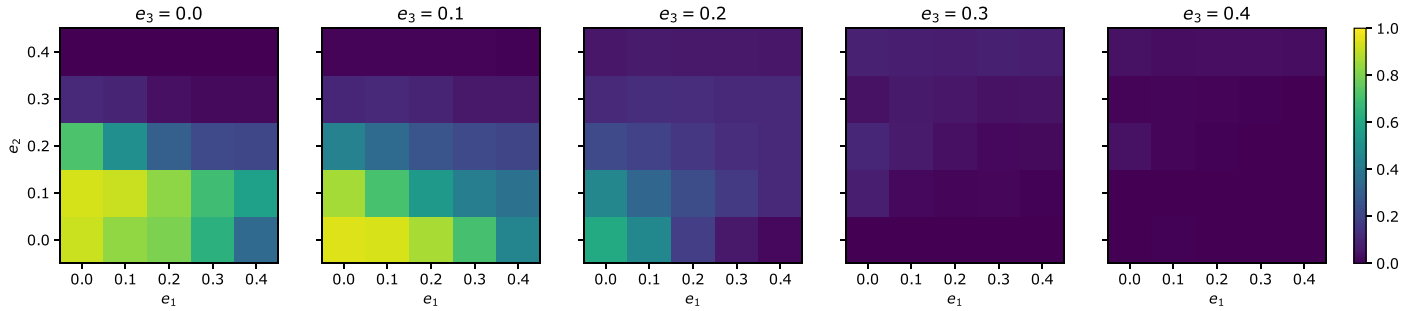

Figure 8. Probability of stability for the GJ 9827 system. We examined the effect of planet eccentricity on the system's stability using `spock`. For each triplet of eccentricities, we vary ω_1, ω_2, and ω_3 from zero to 2π. The color of the box displays the average probability of stability across all ω.

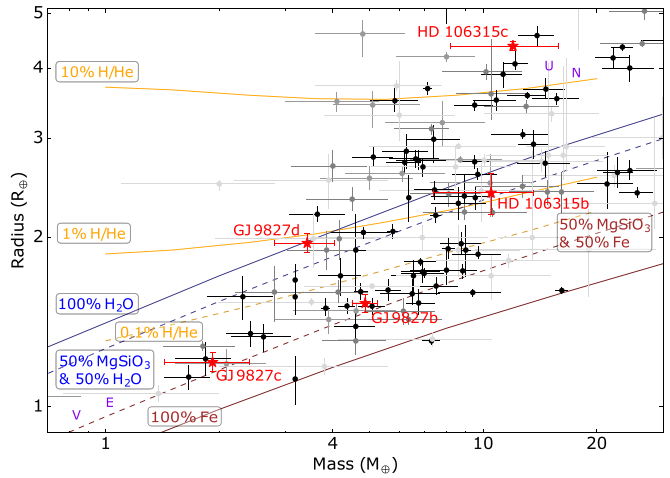

Figure 9. Mass–radius diagram for planets between the size of Earth and Neptune with greater than 2σ measurements (darker points for lower error). The lines show models of different compositions (Lopez & Fortney 2014; Zeng et al. 2016). Our five planets are shown as red stars with 1σ uncertainties.

Table 10
Hydrogen/Helium and Water Mass Fraction Surrounding an Earth-like Core

Planet	$f_{\rm HHe}$ (%)	$f_{\rm H_2O}$ (%)
GJ 9827b	$0.02^{+0.01}_{-0.01}$	$2.20^{+3.84}_{-1.69}$
GJ 9827c	$0.01^{+0.01}_{-0.00}$	$13.57^{+25.18}_{-10.40}$
GJ 9827d	$0.54^{+0.20}_{-0.17}$	$79.10^{+14.35}_{-20.14}$
HD 106315b	$0.96^{+0.72}_{-0.51}$	$54.29^{+29.06}_{-30.09}$
HD 106315c	$12.74^{+1.11}_{-1.06}$	$99.27^{+0.57}_{-1.25}$

calculate the average probability that a given eccentricity pair is stable (Figure 7).

HD 106315 b and HD 106315 c are in relatively close orbits at periods of 9.55 and 21.06 days; their orbits are unstable if either planet has a large eccentricity. The system has a probability of stability greater than 50% when $e_1 \leqslant 0.4$ and $e_2 \leqslant 0.3$; the highest probability of stability is when both planets are in circular orbits.

GJ 9827 b, GJ 9827 c, and GJ 9827 d are in even more closely packed orbits at orbital periods of 1.2, 3.6, and 6.2 days. Therefore, for GJ 9827, we varied e_1, e_2, and e_3 from 0.0 to 0.4 in steps of 0.1 as larger eccentricities for any of the three planets resulted in unstable orbits. At each eccentricity triplet we perform a grid of simulations varying ω_1, ω_2, and ω_3 from zero to 2π in steps of $\frac{\pi}{5}$, creating a total of 125,000 simulations.

We then averaged over the ω grid to calculate the average probability that a given eccentricity triplet is stable (Figure 8).

We find that the GJ 9827 system is unstable if $e_3 \geqslant 0.3$ and the system has very low stability at $e_3 = 0.2$. For $e_3 \leqslant 0.1$, the system can be stable with $e_2 \leqslant 0.2$ and $e_1 \leqslant 0.4$. This system has a smaller range of stable eccentricity values since the planets are packed closer together.

We then convert these eccentricity constraints to secondary eclipse timing constraints (Winn 2010, Equation (33)). We note that the planets in these two systems are not particularly favorable targets for thermal emission spectroscopy based on the emission spectroscopy metric (ESM; Kempton et al. 2018; HD 106315 b: 3; HD 106315 c: 6; GJ 9827 b: 14; GJ 9827 c: 4; and GJ 9827 d: 6).

From our eccentricity constraints and assuming $\omega = 0$, the maximum offsets of the secondary eclipse time for HD 106315 b and HD 106315 c are 2.4 days and 4.0 days respectively. The maximum secondary eclipse timing offsets for the GJ 9827 system are 0.31 days, 0.46 days, and 0.39 days for planet b, c, and d respectively.

6. Interior Bulk Compositions

To explore the interior compositions of these planets, we first visually compare their masses and radii to other known exoplanets on a mass–radius diagram (Figure 9). GJ 9827 b ($\rho_b = 7.5\,{\rm g\,cm^{-3}}$) and GJ 9827 c ($\rho_c = 6.1\,{\rm g\,cm^{-3}}$) are both consistent with a 50/50 mixture of rock and iron. GJ 9827 d ($\rho_d = 2.5\,{\rm g\,cm^{-3}}$) and HD 106315 b ($\rho_b = 4.1\,{\rm g\,cm^{-3}}$) are consistent with either 100% water or a rocky core with a 1% H/He envelope. Lastly, HD 106315 c ($\rho_c = 0.8\,{\rm g\,cm^{-3}}$) is located near our solar system ice giant planets. It has a much lower density than HD 106315 b, too low to be explained by water alone, and is consistent with having a >10% H/He envelope.

To further investigate the interior compositions of these planets, we compared their masses and radii with model composition grids from Zeng & Sasselov (2013), Lopez & Fortney (2014), and Zeng et al. (2016). We focus on two main compositions: Earth-like rock and iron cores surrounded by H/He envelopes and mixtures of water, rock, and iron. Our results are tabulated in Table 10.

To calculate potential H/He mass fractions, we use the grids of thermal evolution models provided by Lopez & Fortney (2014) which calculate the radius of a planet given varying incident fluxes relative to Earth ($S_{inc}/S_\oplus$), masses ($M_p/M_\oplus$), ages, and fractions $f_{\rm HHe}$ of their masses contained in H/He envelopes surrounding Earth-like rock and iron cores. We use the `smint` (Structure Model INTerpolator) interpolation and

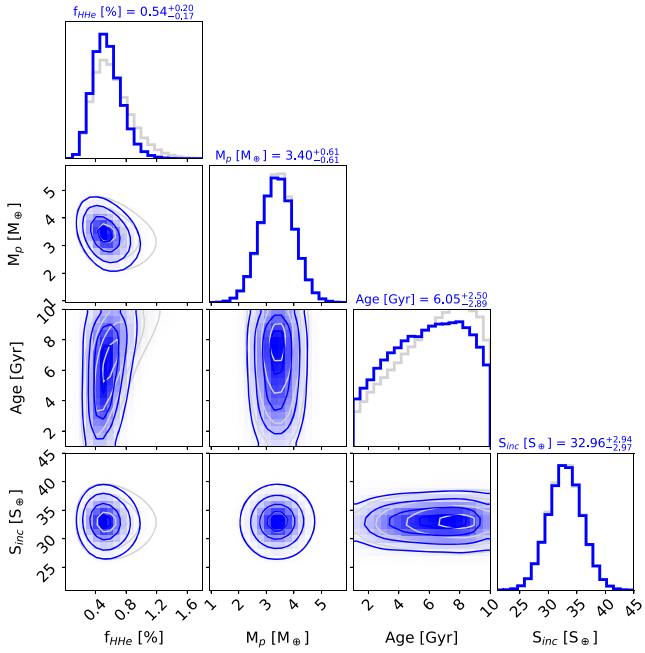

(a) GJ 9827 d

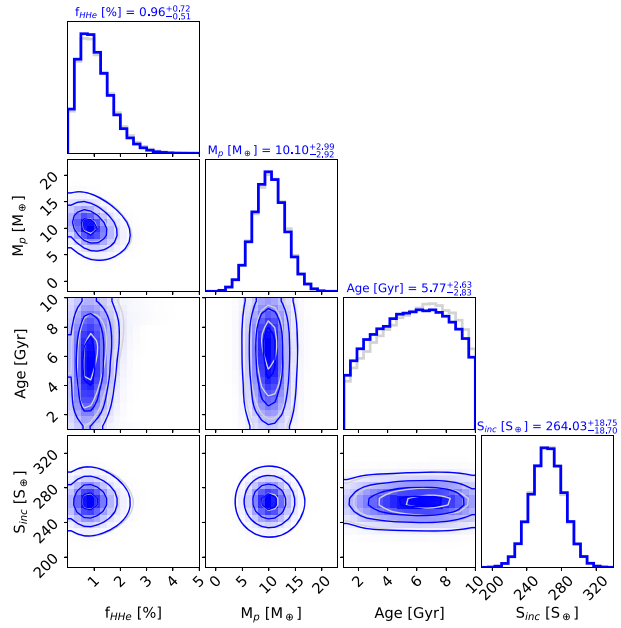

(b) HD 106315 b

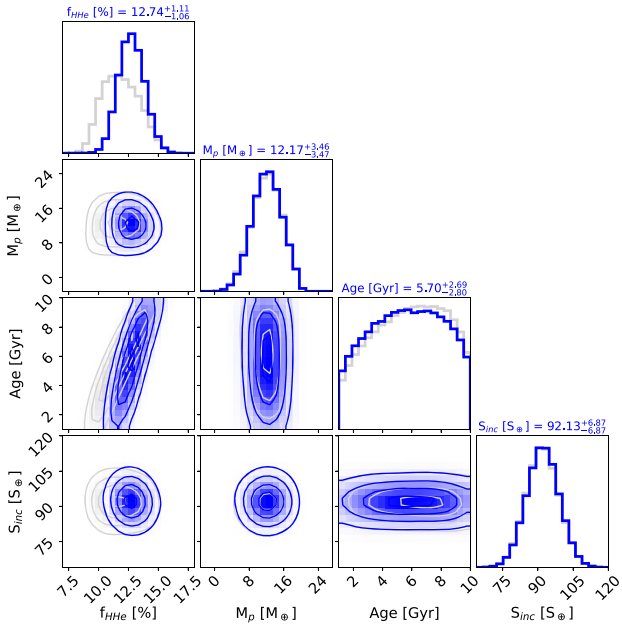

(c) HD 106315 c

Figure 10. Joint and marginalized posterior distributions on the fitted parameters for a 1× (50×) solar metallicity H_2/He envelope atop an Earth-like core are shown in blue (gray). The median and $\pm 1\sigma$ constraints on the parameters for the 1× solar metallicity case are quoted above each marginalized distribution.

envelope mass fraction fitting package, which we made publicly available on GitHub[39], in order to solve the inverse problem of inferring a planet's envelope mass fraction from its incident flux, mass, age, and radius.

`smint` performs linear interpolation over a grid of $f_{\rm HHe}$, $\log_{10} M_p/M_\oplus$, system age, and $\log_{10} S_{inc}/S_\oplus$, and returns the corresponding planet radius. We then run an MCMC that fits for the combination of $S_{\rm inc}$, M_p, age, and $f_{\rm HHe}$ that best matches the observed planet radius. We adopt Gaussian priors on $S_{\rm inc}$ and M_p informed by the stellar and planetary parameters. We use a uniform prior on the planet's envelope mass fraction over the range spanned by the Lopez & Fortney (2014) grids (from 0.1 to 20%) and adopt a uniform prior on the system age from 1 to 10 Gyr. Each of the 100 chains is run for at least 10,000 steps, 60% of which are discarded as burn-in. We make sure that, in each case, the chains have run for at least 50 times the maximum

[39] https://github.com/cpiaulet/smint

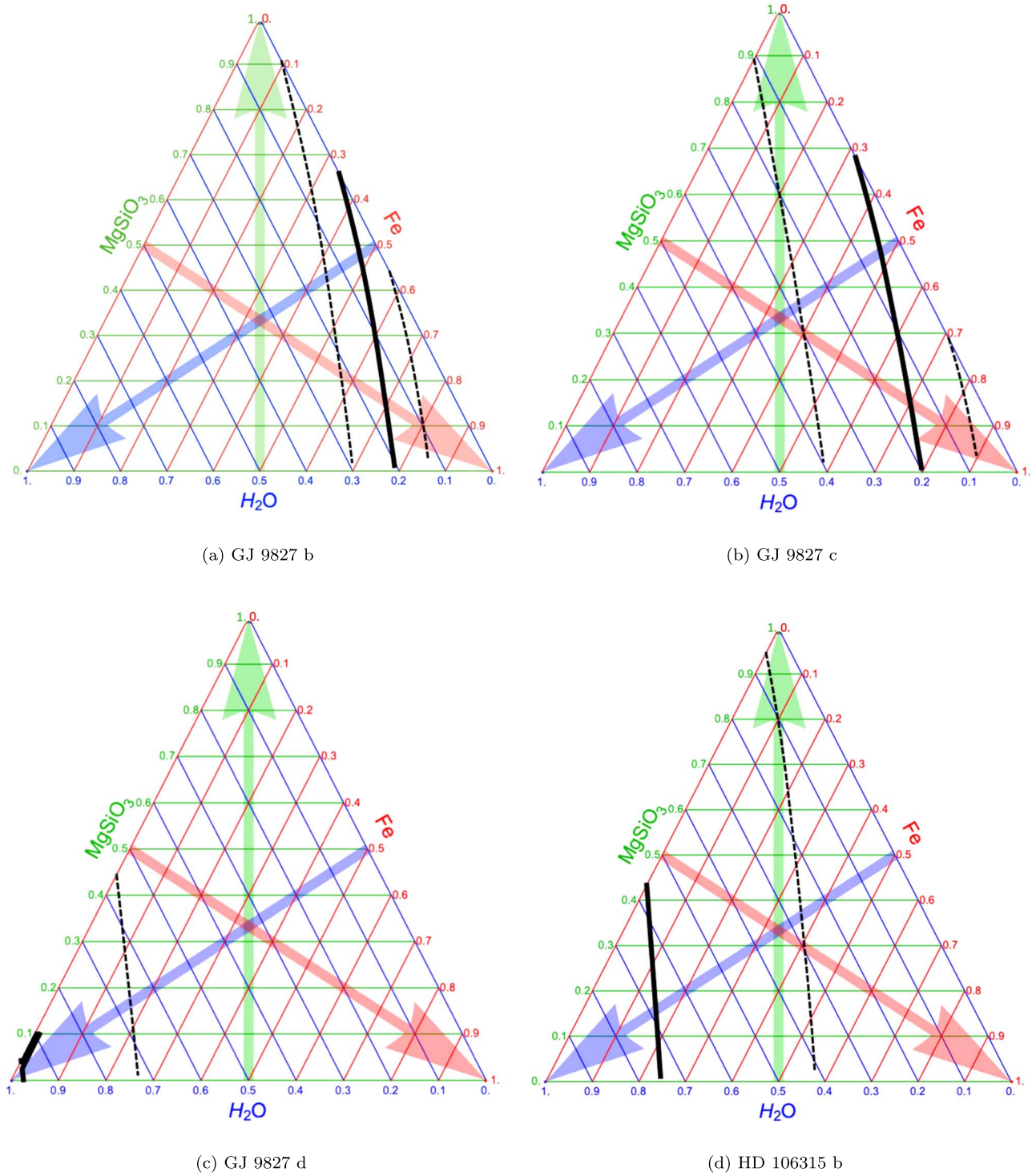

(a) GJ 9827 b

(b) GJ 9827 c

(c) GJ 9827 d

(d) HD 106315 b

Figure 11. Ternary diagrams using a three-component $H_2O/MgSiO_3/Fe$ model (Zeng & Sasselov 2013; Zeng et al. 2016). The solid line outlines the median mass and radius of each planet, while the dashed line(s) delineate the 1σ contours. At any point in the diagram the mass fractions can be found by following the three thin colored lines toward their respective side.

autocorrelation time recorded across all parameters and thus secure that our chains are converged and well sample the posterior probability density functions. We display a corner plot for the three planets consistent with moderate H/He envelopes, GJ 9827 d, HD 106315 b, and HD 106315 c (Figure 10). GJ 9827 d and HD 106315 b are both consistent with 1% H/He envelopes and HD 106315 c is consistent with a 13% H/He envelope.

To fit for the water mass fractions (f_{H_2O}), we use the implementation of the Zeng et al. (2016) two-component (water and rock) model grid in `smint` (Table 10). The MCMC process is analog to that used to fit for f_{HHe}, adopting a uniform prior on the water mass fraction (0%–100%) and a Gaussian prior on the planet mass. We match the observed planet radius via a Gaussian likelihood.

To further investigate the potential f_{H_2O}, we explore three component models of H_2O, $MgSiO_3$, and Fe for four of our planets, excluding HD 106315 c as its low density is inconsistent with these models. We use a numerical tool[40] in order to solve for the interior structure of each planet and produce ternary diagrams of the range of combinations of $MgSiO_3$, Fe, and H_2O mass fractions that are compatible with the observed mass and radius (Zeng & Sasselov 2013; Zeng et al. 2016). These ternary diagrams are shown in Figure 11. GJ 9827 b and GJ 9827 c both have a low H_2O fraction ($\leqslant$40%) and a wide range of possibilities for $MgSiO_3$ and Fe. GJ 9827 d is consistent with a high H_2O fraction (50%–100%) and small fractions of $MgSiO_3$ (0%–50%) and Fe (0%–30%). HD 106315 b is consistent with a wide range for all three components (10%–100% H_2O, 0%–90% $MgSiO_3$, and 0%–60% Fe).

Both Prieto-Arranz et al. (2018) and Rice et al. (2019) suggest that photoevaporation may have sculpted the inner two rocky GJ 9827 planets. However, the outer planet, GJ 9827 d, must have retained a moderate fraction of volatiles to be consistent with its mass and radius. We examine whether the system as a whole is consistent with the theory of photoevaporation through calculating the minimum mass required of planet d to retain its atmosphere assuming planets b and c lost theirs to photoevaporation, as described in Owen & Campos Estrada (2019). We find the minimum mass for GJ 9827 d is 1 $M_\oplus$, lower than its mass of 3.3 $M_\oplus$. Therefore, this system is in agreement with this photoevaporation model (Owen & Wu 2013, 2017). Although, GJ 9827 d may have had a different type of atmospheric evolution other than photoevaporation. Kasper et al. (2020) set stringent limits on the presence of any extended atmosphere around GJ 9827 d via high-resolution spectroscopy of the metastable 10,833 ÅHe triplet, inconsistent with current models of atmospheric formation and mass loss.

Furthermore, the three GJ 9827 planets span the radius gap at $1.7R_\oplus$(Fulton et al. 2017). The inner two planets are high density and smaller than the radius gap ($R_b = 1.5R_\oplus$, $R_c = 1.2R_\oplus$) whereas the outer planet is lower density and larger than the radius gap ($R_d = 2.0R_\oplus$). HD 106315 b and c are both lower density and larger than the radius gap ($R_b = 2.4R_\oplus$, $R_c = 4.4R_\oplus$). The five planets in these systems agree with a theory that planets smaller than $1.7R_\oplus$ are primarily composed of rocky cores and larger planets have additional volatile material that contributes to their radii (Weiss et al. 2016; Fulton et al. 2017).

7. Conclusion

In this paper, we characterized two systems, HD 106315 and GJ 9827. These bright stars host super-Earth and sub-Neptune planets well suited for atmospheric characterization by HST and JWST. From our Spitzer analysis (Section 2) we improved the planets' ephemerides, enabling accurate transit prediction required for future atmospheric characterization through transmission spectroscopy. We incorporated Gaia parallaxes to update the stellar parameters for both systems and further constrained the limiting magnitude of nearby companions to HD 106315 through imaging data (Section 3).

As the results of a multiyear high-cadence observing campaign with Keck/HIRES and Magellan/PFS, we improved the planet's mass measurements in preparation for the interpretation of HST transmission spectra. We measured planet masses in the GJ 9827 system to be $M_b = 4.87 \pm 0.37$ $M_\oplus$, $M_c = 1.92 \pm 0.49$ $M_\oplus$, and $M_d = 3.42 \pm 0.62$ $M_\oplus$. For HD 106315, we found planet masses of $M_b = 10.5 \pm 3.1$ $M_\oplus$ and $M_c = 12.0 \pm 3.8$ $M_\oplus$. Atmospheric characterization of small planets benefits from mass detections at 5σ significance (Batalha et al. 2019). We have achieved 5σ masses for two planets with pending HST analyses, GJ 9827 b and GJ 9827 d (Hedges et al. 2020, in preparation, Benneke et al. 2020, in preparation), and a 4σ mass for the third, HD 106315 c (Kreidberg et al. 2020).

For GJ 9827, stellar activity signatures in the photometry and Calcium II H&K lines (Section 4) informed our use of a Gaussian process to account for this activity in our radial velocity fit. We did not adopt the Gaussian process fit for our HD 106315 analysis due to the higher AIC value and the lack of activity signatures seen in the Calcium II H&K lines and radial velocity data. Hotter stars ($T_{\rm eff} > 6200$ K) often have shallow convective envelopes and inefficient magnetic dynamos which result in fewer spots on the stellar surface (Kraft 1967). Therefore, hotter stars like HD 106315 may not have enough starspots for this type of Gaussian process to be effective.

We additionally explored the possible eccentricities for these planets through stability arguments. We found that low eccentricities are required for stability for these two closely packed systems. We finally compared our derived masses and densities with previously published models to investigate interior compositions for these planets. We found that GJ 9827 b and GJ 9827 c are both consistent with a 50/50 rock-iron composition, GJ 9827 d and HD 106315 b both require additional volatiles, and HD 106315 c is consistent with a $\sim$10% by mass hydrogen/helium envelope.

We thank the anonymous reviewer for their time and helpful comments.

M.R.K is supported by the NSF Graduate Research Fellowship, grant No. DGE 1339067.

C.P. is supported by the Technologies for Exo-Planetary Science (TEPS) CREATE program and further acknowledges financial support by the Fonds de Recherche QuébécoisNature et Technologie (FRQNT; Québec).

G.W.H. acknowledges long-term support from NASA, NSF, Tennessee State University, and the State of Tennessee through its Centers of Excellence program.

L.M.W. is supported by the Beatrice Watson Parrent Fellowship and NASA ADAP grant 80NSSC19K0597.

P.D. acknowledges support from a National Science Foundation Astronomy and Astrophysics Postdoctoral Fellowship under award AST-1903811.

J.M.A.M. gratefully acknowledges support from the National Science Foundation Graduate Research Fellowship Program under grant No. DGE-1842400. J.M.A.M. also thanks the LSSTC Data Science Fellowship Program, which is funded by LSSTC, NSF Cybertraining grant No. 1829740, the Brinson Foundation, and the Moore Foundation; his participation in the program has benefited this work.

The authors wish to recognize and acknowledge the very significant cultural role and reverence that the summit of Maunakea has always had within the indigenous Hawaiian community. We are most fortunate to have the opportunity to conduct observations from this mountain.

[40] https://www.cfa.harvard.edu/~lzeng

Some of the observations in the paper made use of the High-Resolution Imaging instrument Zorro. Zorro was funded by the NASA Exoplanet Exploration Program and built at the NASA Ames Research Center by Steve B. Howell, Nic Scott, Elliott P. Horch, and Emmett Quigley. Zorro is mounted on the Gemini South telescope of the international Gemini Observatory, a program of NSFs OIR Lab, which is managed by the Association of Universities for Research in Astronomy (AURA) under a cooperative agreement with the National Science Foundation.

This work is based in part on observations made with the Spitzer Space Telescope, which was operated by the Jet Propulsion Laboratory, California Institute of Technology under a contract with NASA. Support for this work was provided by NASA through an award issued by JPL/Caltech.

This research has made use of the Exoplanet Follow-up Observing Program (ExoFOP), which is operated by the California Institute of Technology, under contract with the National Aeronautics and Space Administration.

Part of the research was carried out at the Jet Propulsion Laboratory, California Institute of Technology, under a contract with the National Aeronautics and Space Administration (80NM0018D0004).

This work has made use of data from the European Space Agency (ESA) mission Gaia (https://www.cosmos.esa.int/gaia), processed by the Gaia Data Processing and Analysis Consortium (DPAC, https://www.cosmos.esa.int/web/gaia/dpac/consortium). Funding for the DPAC has been provided by national institutions, in particular the institutions participating in the Gaia Multilateral Agreement.

Facilities: Keck:I(HIRES), Magellan:Clay(PFS), Spitzer, APF, TSU:AIT, Gemini:South(Zorro).

Software: `radvel` (Fulton et al. 2018), `batman` (Kreidberg 2015), `SpecMatch-Emp` (Yee et al. 2017), `isoclassify` (Huber et al. 2017), `spock` (Tamayo et al. 2020), `rebound` (Rein & Liu 2011), `numpy` (van der Walt et al. 2011), `astropy` (Astropy Collaboration et al. 2013), `emcee` (Foreman-Mackey et al. 2013).

ORCID iDs

Molly R. Kosiarek https://orcid.org/0000-0002-6115-4359
David A. Berardo https://orcid.org/0000-0001-6298-412X
Cesar Laguna https://orcid.org/0000-0003-1314-7514
Caroline Piaulet https://orcid.org/0000-0002-2875-917X
Joseph M. Akana Murphy https://orcid.org/0000-0001-8898-8284
Steve B. Howell https://orcid.org/0000-0002-2532-2853
Gregory W. Henry https://orcid.org/0000-0003-4155-8513
Howard Isaacson https://orcid.org/0000-0002-0531-1073
Benjamin Fulton https://orcid.org/0000-0003-3504-5316
Lauren M. Weiss https://orcid.org/0000-0002-3725-3058
Erik A. Petigura https://orcid.org/0000-0003-0967-2893
Aida Behmard https://orcid.org/0000-0003-0012-9093
Lea A. Hirsch https://orcid.org/0000-0001-8058-7443
Jennifer A. Burt https://orcid.org/0000-0002-0040-6815
Sean M. Mills https://orcid.org/0000-0002-4535-6241
Ashley Chontos https://orcid.org/0000-0003-1125-2564
Teo Močnik https://orcid.org/0000-0003-4603-556X
Andrew W. Howard https://orcid.org/0000-0001-8638-0320
Michael Werner https://orcid.org/0000-0003-4990-189X
John H. Livingston https://orcid.org/0000-0002-4881-3620
Jessica Krick https://orcid.org/0000-0002-2413-5976
Charles Beichman https://orcid.org/0000-0002-5627-5471
Varoujan Gorjian https://orcid.org/0000-0002-8990-2101
Laura Kreidberg https://orcid.org/0000-0003-0514-1147
Caroline Morley https://orcid.org/0000-0002-4404-0456
Jessie L. Christiansen https://orcid.org/0000-0002-8035-4778
Farisa Y. Morales https://orcid.org/0000-0001-9414-3851
Nicholas J. Scott https://orcid.org/0000-0003-1038-9702
Jeffrey D. Crane https://orcid.org/0000-0002-5226-787X
Sharon Xuesong Wang https://orcid.org/0000-0002-6937-9034
Lee J. Rosenthal https://orcid.org/0000-0001-8391-5182
Samuel K. Grunblatt https://orcid.org/0000-0003-4976-9980
Ryan A. Rubenzahl https://orcid.org/0000-0003-3856-3143
Paul A. Dalba https://orcid.org/0000-0002-4297-5506
Steven Giacalone https://orcid.org/0000-0002-8965-3969
Fei Dai https://orcid.org/0000-0002-8958-0683
Michelle L. Hill https://orcid.org/0000-0002-0139-4756
Malena Rice https://orcid.org/0000-0002-7670-670X
Stephen R. Kane https://orcid.org/0000-0002-7084-0529
Andrew W. Mayo https://orcid.org/0000-0002-7216-2135

References

Albrecht, S., Winn, J. N., Marcy, G. W., et al. 2013, ApJ, 771, 11
Astropy Collaboration, Robitaille, T. P., Tollerud, E. J., et al. 2013, A&A, 558, A33
Barros, S. C. C., Gosselin, H., Lillo-Box, J., et al. 2017, A&A, 608, A25
Batalha, N. E., Lewis, T., Fortney, J. J., et al. 2019, ApJL, 885, L25
Berardo, D., Crossfield, I. J. M., Werner, M., et al. 2019, AJ, 157, 185
Butler, R. P., Marcy, G. W., Williams, E., et al. 1996, PASP, 108, 500
Chaplin, W. J., Cegla, H. M., Watson, C. A., Davies, G. R., & Ball, W. H. 2019, AJ, 157, 163
Claret, A., & Bloemen, S. 2011, A&A, 529, A75
Crane, J. D., Shectman, S. A., & Butler, R. P. 2006, Proc. SPIE, 6269, 626931
Crane, J. D., Shectman, S. A., Butler, R. P., et al. 2010, Proc. SPIE, 7735, 773553
Crane, J. D., Shectman, S. A., Butler, R. P., Thompson, I. B., & Burley, G. S. 2008, Proc. SPIE, 7014, 701479
Crossfield, I. J. M., Ciardi, D. R., Isaacson, H., et al. 2017, AJ, 153, 255
Deming, D., Knutson, H., Kammer, J., et al. 2015, ApJ, 805, 132
Eaton, J. A., Henry, G. W., & Fekel, F. C. 2003, ASSL, 288, 189
Fazio, G. G., Hora, J. L., Allen, L. E., et al. 2004, ApJS, 154, 10
Figueira, P., Pont, F., Mordasini, C., et al. 2009, A&A, 493, 671
Foreman-Mackey, D., Hogg, D. W., Lang, D., & Goodman, J. 2013, PASP, 125, 306
Frandsen, S., & Lindberg, B. 1999, in Astrophysics with the NOT, ed. H. Karttunen & V. Piirola (Piikkio: Univ. Turku), 71
Fulton, B. J., Petigura, E. A., Blunt, S., & Sinukoff, E. 2018, PASP, 130, 044504
Fulton, B. J., Petigura, E. A., Howard, A. W., et al. 2017, AJ, 154, 109
Fulton, B. J., Weiss, L. M., Sinukoff, E., et al. 2015, ApJ, 805, 175
Gaia Collaboration, Brown, A. G. A., Vallenari, A., et al. 2018, A&A, 616, A1
Gaia Collaboration, Prusti, T., de Bruijne, J. H. J., et al. 2016, A&A, 595, A1
Haywood, R. D., Collier Cameron, A., Queloz, D., et al. 2014, MNRAS, 443, 2517
Henry, G. W. 1999, PASP, 111, 845
Howard, A. W., Johnson, J. A., Marcy, G. W., et al. 2010, ApJ, 721, 1467
Howell, S. B., Everett, M. E., Sherry, W., Horch, E., & Ciardi, D. R. 2011, AJ, 142, 19
Huber, D., Zinn, J., Bojsen-Hansen, M., et al. 2017, ApJ, 844, 102
Isaacson, H., & Fischer, D. 2010, ApJ, 725, 875
Kasper, D., Bean, J. L., Oklopčić, A., et al. 2020, AJ, 160, 258
Kempton, E. M. R., Bean, J. L., Louie, D. R., et al. 2018, PASP, 130, 114401
Kosiarek, M. R., & Crossfield, I. J. M. 2020, AJ, 159, 271
Kraft, R. P. 1967, ApJ, 150, 551
Kreidberg, L. 2015, PASP, 127, 1161
Kreidberg, L., Mollière, P., Crossfield, I. J. M., et al. 2020, arXiv:2006.07444
Lendl, M., Ehrenreich, D., Turner, O. D., et al. 2017, A&A, 603, L5

Lopez, E. D., & Fortney, J. J. 2014, ApJ, 792, 1
Luri, X., Brown, A. G. A., Sarro, L. M., et al. 2018, A&A, 616, A9
Mayor, M., Pepe, F., Queloz, D., et al. 2003, Msngr, 114, 20
Nava, C., López-Morales, M., Haywood, R. D., & Giles, H. A. C. 2020, AJ, 159, 23
Niraula, P., Redfield, S., Dai, F., et al. 2017, AJ, 154, 266
Owen, J. E., & Campos Estrada, B. 2019, MNRAS, 491, 5287
Owen, J. E., & Wu, Y. 2013, ApJ, 775, 105
Owen, J. E., & Wu, Y. 2017, ApJ, 847, 29
Petigura, E. A., Howard, A. W., Marcy, G. W., et al. 2017, AJ, 154, 107
Petigura, E. A., Schlieder, J. E., Crossfield, I. J. M., et al. 2015, ApJ, 811, 102
Prieto-Arranz, J., Palle, E., Gandolfi, D., et al. 2018, A&A, 618, A116
Radovan, M. V., Lanclos, K., Holden, B. P., et al. 2014, Proc. SPIE, 9145, 91452B
Rein, H., & Liu, S.-F. 2011, REBOUND: Multi-purpose N-body Code for Collisional Dynamics, Astrophysics Source Code Library, ascl:1110.016
Rice, K., Malavolta, L., Mayo, A., et al. 2019, MNRAS, 484, 3731
Robertson, P., Endl, M., Cochran, W. D., & Dodson-Robinson, S. E. 2013, ApJ, 764, 3
Rodriguez, J. E., Vanderburg, A., Eastman, J. D., et al. 2018, AJ, 155, 72
Rodriguez, J. E., Zhou, G., Vanderburg, A., et al. 2017, AJ, 153, 256
Rogers, L. A., & Seager, S. 2010, ApJ, 712, 974
Tamayo, D., Cranmer, M., Hadden, S., et al. 2020, PNAS, 117, 18194
Telting, J. H., Avila, G., Buchhave, L., et al. 2014, AN, 335, 41
Teske, J. K., Wang, S., Wolfgang, A., et al. 2018, AJ, 155, 148
van der Walt, S., Colbert, S. C., & Varoquaux, G. 2011, CSE, 13, 22
Vogt, S. S., Allen, S. L., Bigelow, B. C., et al. 1994, Proc. SPIE, 2198, 362
Vogt, S. S., Radovan, M., Kibrick, R., et al. 2014, PASP, 126, 359
Weiss, L. M., Rogers, L. A., Isaacson, H. T., et al. 2016, ApJ, 819, 83
Winn, J. N. 2010, in Exoplanets, ed. S. Seager (Tucson, AZ: Univ. Arizona Press), 55
Yee, S. W., Petigura, E. A., & von Braun, K. 2017, ApJ, 836, 77
Zeng, L., & Sasselov, D. 2013, PASP, 125, 227
Zeng, L., Sasselov, D. D., & Jacobsen, S. B. 2016, ApJ, 819, 127
Zhou, G., Rodriguez, J. E., Vanderburg, A., et al. 2018, AJ, 156, 93